Dense gas flow simulations in ultra-tight confinement

Dense gas flow simulations in ultra-tight confinement

Qiang Sheng,[1] Livio Gibelli,[1] Jun Li,[2, a)] Matthew K. Borg,[1, b)] and Yonghao Zhang[3]
[1)]*School of Engineering, University of Edinburgh, Edinburgh EH9 3FB, UK*
[2)]*Center for Integrative Petroleum Research, College of Petroleum Engineering and Geosciences, King Fahd University of Petroleum and Minerals, Dhahran 31261, Saudi Arabia*
[3)]*James Weir Fluids Laboratory, Department of Mechanical and Aerospace Engineering, University of Strathclyde, Glasgow G1 1XJ, UK*

(Dated: 10 August 2020)

Modelling dense gas flows inside channels with sections comparable to the diameter of gas molecules is essential in porous media applications, such as in non-conventional shale reservoir management and nanofluidic separation membranes. In this paper, we perform the first verification study of the Enskog equation by using particle simulation methods based on the same hard-sphere collisions dynamics. Our in-house Event-Driven Molecular Dynamics (EDMD) code and a pseudo-hard-sphere Molecular Dynamics (PHS-MD) solver are used to study force-driven Poiseuille flows, in the limit of high gas densities and high confinements. Our results showed (a) very good agreement between EDMD, PHS-MD, and Enskog solutions across density, velocity, and temperature profiles for all the simulation conditions, and (b) numerical evidence that deviations exist in the normalized mass flow rate versus Knudsen number curve compared to the standard curve without confinement. While we observe slight deviations in the Enskog density and velocity profiles from the MD when the reduced density is greater than 0.2, this limit is well above practical engineering applications, such as in shale gas. The key advantages of promoting the Enskog equation for upscaling flows in porous media lie in its ability to capture the non-equilibrium physics of tightly confined fluids, while being computationally more efficient than fundamental simulation approaches, such as molecular dynamics and derivative solvers.

I. INTRODUCTION

Gas transport in nano/microscale channels, such as in nanotube membranes[1] or porous rock[2] presents a serious modelling challenge. In these application problems, the underlying assumptions of conventional fluid mechanics — the requirements of local thermodynamic equilibrium — break down, which limits the applicability of computational fluid dynamics (CFD) solvers, such as the Navier-Stokes-Fourier (NSF) equations. In microscale geometries, it is a well known fact that a gas experiences a degree of rarefaction when its molecular mean free path λ, which is on the order of tens of nanometres at standard atmospheric conditions, becomes comparable to the characteristic lengthscale of the flow H (e.g. the channel height). This degree of rarefaction is caused by insufficient intermolecular collisions and can be characterised by the Knudsen number, $Kn = \lambda/H$. The continuum approach can be safely applied for $Kn < 0.001$, while larger Knudsen numbers describe the non-continuum regimes of slip flow ($0.001 < Kn < 0.1$), transition flow ($0.1 < Kn < 10$) and free-molecular flow ($Kn > 10$).

In the slip flow regime, the predictions from the NSF equations can be improved by using velocity/thermal slip boundary conditions[3–5], while the extended hydrodynamic equations[6,7] can model rarefied flows in the early transition regime. Numerical solutions of the Boltzmann equation based on stochastic particle schemes[8–12] and deterministic integration methods[13,14], have successfully been used to model the full range of Knudsen numbers in the non-continuum regimes.

For these microscale geometries, the Knudsen "paradox" describes the flow response to a pressure-drop in a parallel-plate geometry subjected to different rarefaction[15]. Starting from the continuum limit, and increasing the Knudsen number, the mass flow rate through a channel is observed to drop due to a decrease in viscous diffusivity until around the transition regime, where the flow rate starts to increase again, caused by the dominant gas-wall collisions (i.e. the Knudsen diffusivity)[16,17].

For nanoscale geometries, however, the channel height becomes comparable to the diameter of the gas molecule σ. These ultra-tight channel problems invalidate the use of the Boltzmann equation central to the above methods. When the average distance between molecules is of the order of σ, their space correlations need to be taken into account and lead to effects which cannot be captured by kinetic equations developed for dilute gases, like molecular ordering near walls[18] and non-local transport coefficients[19–22].

[a)]Electronic mail: junli@kfupm.edu.sa
[b)]Electronic mail: matthew.borg@ed.ac.uk

While some experiments of gas flows exist for nanostructured membranes, such as graphene oxide layers or carbon nanotubes[1,23,24], due to the extreme small scales, these are normally challenging to perform accurately and are very limited in data. This means we need to continue to develop better computational methods to enable new scientific insights.

In principle, the Enskog equation can be used to extend the kinetic theory description of fluids to densities beyond the dilute-gas Boltzmann limit[25]. While keeping binary collision dynamics, atoms are no longer treated as dimensionless points, as in the Boltzmann approach, and the finite-size effects are accounted for by including the space correlations between colliding molecules into the modelling, the molecular mutual shielding, and the reduction of the volume available to molecules. The Enskog equation has been used over the years to study the properties of a hard-sphere dense gas near the solid walls of micro and nano-channels[26–28] and its extension to systems of weakly attracting hard-spheres has successfully been used to describe liquid-vapor flows[29–31], and the formation and breakage of liquid menisci in nanochannels[32].

Molecular dynamics (MD) and other particle computational tools, such as event-driven MD (EDMD), provide a more fundamental description of the fluid behaviour at the nanoscale. These techniques model the Newtonian dynamics of individual atoms and their collisions through potential energy functions, such as Lennard Jones for smooth interactions[33,34] or hard-sphere interactions for EDMD[35]. These particle-based approaches have been the dominant modelling route of high-confined fluids[36–42], although have mainly focussed on equilibrium properties and flow profiles of the tight confinement, rather than on the overall gas-flow response, which we cover in this paper.

The major barrier in MD as a simulation method lies in its poor scale up; it would be computationally intractable to simulate larger complex 3D porous media. In this regard, the use of the Enskog equation is attractive because it reduces the computational burden by avoiding the detailed computation of the atoms' dynamics, but its capability of capturing the fluid behaviour in confined geometries needs to be more extensively assessed.

In a recent work[43], one of the authors of this paper found that dense gas flows under tight confinement deviated substantially from the classical Knudsen minimum curve for the flow response described earlier, and the Knudsen minimum is observed to disappear for flows at the highest confinement. However, these results were not validated with other methods.

The scope and novelty of this paper is twofold: (a) to verify the overall picture of the flow responses under various Knudsen numbers for dense gases subject to ultra-tight confinement, and (b) to rigorously assess the accuracy of the Enskog solutions, by using independent high-fidelity molecular dynamics simulations with an identical collision model and boundary conditions. The rest of the paper is organised as follows. The simulation details are introduced in Section II and results presented in Section III. We conclude and give an overview of where we envisage this work will be heading in Section IV.

II. COMPUTATIONAL METHODS

A. Simulation details

Force-driven Poiseuille flow between two infinite parallel plates is considered in this work, using three independent computational models: a) an Enskog solver, b) an Event Driven Molecular Dynamics (EDMD) solver and c) a pseudo-hard-sphere Molecular Dynamics (PHS-MD) solver. The details of these three methods are given in the next sections.

The geometry, collisional model, and boundary conditions are kept the same across the three models. The case set-up consists of a channel of height H between the two plates in the z direction, and periodic boundary conditions in both the flow direction x, and the transverse-flow direction y. The channel lengths in the x, y directions are chosen to improve statistics in the flow measurements, and may be different across cases. All walls are described as mathematical walls, which are maintained at a fixed temperature T_{wall} and modelled as fully diffusive boundary conditions, i.e. atoms are supposed to be re-emitted according to the Maxwell scattering kernel with complete accommodation[3]. No temperature control in the bulk of the fluid is applied during the main simulation run, as this would be an outcome from the balance between viscous dissipation and thermalisation at the walls. All collisions consider a hard-sphere implementation and, as such, collisions between particles and the walls occur at the circumference of the particle, and not at its midpoint. We define our parametric space using two dimensionless parameters: the confinement ratio R and the reference reduced density η_0. The confinement ratio is $R = H/\sigma$, and defines the degree of scale separation between the gas atom diameter σ and the channel height. In this work, changes in R were adjusted by changes in H only. Gas flows with the following different confinement ratios are investigated: R = 2, 3, 5, 10 and 20. The reference reduced density is given by $\eta_0 = n_0\pi\sigma^3/6$, where n_0 is the fluid reference number density, and defines the packing fraction of gas atoms within the fluid volume.

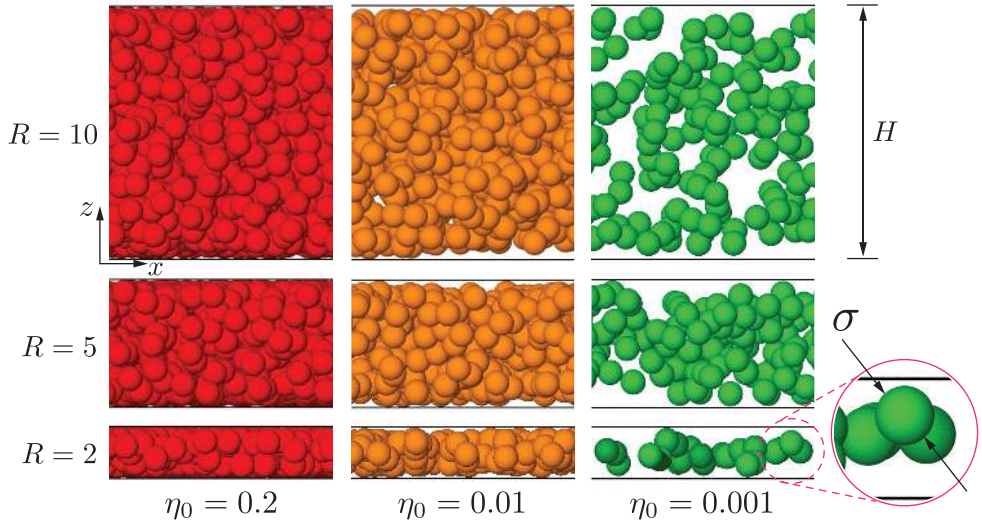

FIG. 1. Poiseuille flow set-up for all three models. Examples shown for three reference reduced densities η_0, and three confinements R. The channel height H is defined in the z direction from the solid black lines, while flow is driven in the x direction by a body force. Note, only small slices of the case setups are shown in this figure; these simulation domains are much larger in the x direction in order to improve the statistics in the measurements.

Gas flows are then investigated with reference reduced densities in the range $\eta_0 = [0.0005, 0.3]$, as shown in Table II A. Note that the Knudsen number depends on the confinement ratio *and* the reference reduced density through the relationship

$$Kn = \frac{1}{6\sqrt{2}} \frac{1}{\eta_0 \chi(\eta_0)} \frac{1}{R}, \tag{1}$$

where χ is the contact value of the pair correlation function in a hard-sphere fluid in uniform equilibrium[3]. An expression for χ can be obtained from the equation of state of the hard-sphere fluid proposed by Carnahan and Starling[44], as

$$\chi(\eta) = \frac{1}{2} \frac{2-\eta}{(1-\eta)^3}. \tag{2}$$

In order to simulate the force-driven Poiseuille flow, a force $\tilde{F} = F\sigma/k_BT$ is applied to each atom, where F is the force in dimensional units and k_B is the Boltzmann constant. Any measurements of flow are only performed after the fluid reaches a steady state.

			Kn				
η_0	p_0	μ_0	R=2	R=3	R=5	R=10	R=20
0.0001	0.02	1.0001	–	–	–	–	–
0.0002	0.04	1.0001	–	–	–	–	29.453
0.0005	0.1	1.0004	–	–	–	23.544	11.772
0.001	0.2	1.0007	58.788	39.192	23.515	11.757	5.879
0.005	1.0	1.0039	11.640	7.760	4.656	2.328	1.164
0.010	2.0	1.0084	5.747	3.832	2.299	1.149	0.575
0.050	12.2	1.0747	1.037	0.691	0.415	0.207	0.104
0.100	30.2	1.2492	0.452	0.302	0.181	0.090	0.045
0.200	95.0	2.0819	0.168	0.112	0.067	0.034	0.017
0.300	231.0	4.1327	0.079	0.053	0.032	0.016	0.005

TABLE I. Variation of Knudsen number Kn with reference reduced density η_0 and confinement ratios R considered in this work. Also shown are the reference dimensional pressure p_0 (MPa) and dimensionless reference viscosity μ_0 (normalized by the viscosity of the hard-sphere system $\mu_{HS} = (5/16\sigma^2)\sqrt{mk_BT/\pi}$), which are calculated from η_0.

B. Enskog solver

The kinetic theory description of fluids is statistical in nature and it is based on the molecular velocity distribution function $f = f(\boldsymbol{r}, \boldsymbol{v}, t)$, defined as the number of atoms in the element of volume $d\boldsymbol{r}$ around $\boldsymbol{r}$, having velocities in the range $\boldsymbol{v}$ to $\boldsymbol{v} + d\boldsymbol{v}$. The Enskog equation describes the space and time evolution of f for a dense gas, i.e. a gas in which the effects of the finite size of atoms and non-local collisions play a prominent role,

$$\frac{\partial f}{\partial t} + \boldsymbol{v} \cdot \frac{\partial f}{\partial \boldsymbol{r}} = \sigma^2 \int (\boldsymbol{v}_r \cdot \hat{\boldsymbol{k}})^+ d\boldsymbol{v}_1 d^2\hat{\boldsymbol{k}} \Big\{ \chi[\eta](\boldsymbol{r}, \boldsymbol{r} + \sigma\hat{\boldsymbol{k}}) f(\boldsymbol{r} + \sigma\hat{\boldsymbol{k}}, \boldsymbol{v}_1^*, t) f(\boldsymbol{r}, \boldsymbol{v}^*, t) - \chi[\eta](\boldsymbol{r}, \boldsymbol{r} - \sigma\hat{\boldsymbol{k}}) f(\boldsymbol{r} - \sigma\hat{\boldsymbol{k}}, \boldsymbol{v}_1, t) f(\boldsymbol{r}, \boldsymbol{v}, t) \Big\}, \tag{3}$$

where σ is the molecular diameter, v_r is the relative velocity of the colliding atoms, $\hat{k}$ is the unit vector associated to their relative positions at the time of the impact, (v^*, v_1^*) are the pre-collisional velocities, which are transformed into the post-collisional velocities (v, v_1) by the hard-sphere collision dynamics rules, and η is the reduced density. In the framework of the so-called standard Enskog theory (SET), χ is simply set equal to the equilibrium pair correlation function taken at the midpoint of the line joining the centers of colliding atoms, while in the revised Enskog theory (RET) the local value of the non-equilibrium pair correlation function is used instead[45]. The RET was found to possess better theoretical properties, but it is mathematically more complicated and its numerical solution is more involved, albeit feasible.

In the present work, the SET was used and, following the Fischer-Methfessel approach[46], the actual value of the density at the contact point is replaced with the value of the density field averaged over a spherical volume of diameter σ, namely:

$$\chi[\eta](r, r \pm \sigma\hat{k}) = \chi\left[\overline{\eta}\left(r \pm \sigma\frac{\hat{k}}{2}\right)\right], \qquad (4)$$

where χ is given by Eq. (2) and

$$\overline{\eta}(r,t) = \frac{3}{4\pi\sigma^3}\int_{\mathbb{R}^3} \eta(r_*,t) w(r, r_*)\, dr_*, \qquad (5)$$

$$w(r, r_*) = \begin{cases} 1, & \|r_* - r\| < \sigma \\ 0, & \|r_* - r\| > \sigma \end{cases}. \qquad (6)$$

The Enskog equation was solved by a particle method, which is an extension of the classical direct simulation Monte Carlo (DSMC) for dilute gases[47]. In this numerical scheme, the main framework of DSMC is preserved, with modifications occurring in the collision algorithm due to the non-local structure of the Enskog collision integral, i.e. the right hand side of Eq. (3). The velocity distribution function of the fluid atoms is represented by computational particles whose number was set to 2×10^6 and made equal to the number of real atoms by a proper choice of the cross section normal to the non-homogeneous direction z. The one-dimensional computational domain was divided into a number of cells of equal size, not exceeding $\Delta z = \sigma/10$. Particles' motion and interactions are decoupled over a time step Δt, which was set significantly shorter than the local mean free time between collisions, namely $10^{-3}\sqrt{\sigma^2 m/k_B T}$. In each time-step, the particles are first translated as if they do not interact with each other. Note that the overlapping between atom spheres may occur as a consequence of this movement. During this step, diffuse reflections were applied to describe the scattering of atoms impinging on the channel solid walls. Afterwards, collisions are evaluated according to stochastic rules, which essentially correspond to the Monte Carlo evaluation of the Enskog collision integral. Note that, unlike DSMC, collisions in general involve closest neighbour cells due to the non-local structure of the Enskog collision integral. The simulation was followed until a steady state was formed, by letting the transient behaviour evolve into a time-independent solution. The calculation of the macroscopic quantities commenced after the steady state has been reached through weighted averages of the particles properties, with the sampling time duration determined by requiring that the relative statistical error does not exceed 2%.

C. EDMD solver

Molecular dynamics simulations for discrete potential systems are not as prevalent as for continuous potential systems, but an extensive literature has been developed over the years[48–50]. Discrete potentials have been shown to both approximate soft potentials[51] and directly reproduce thermodynamic data[52]. Their main benefit is that they lead to simulations far more computationally efficient than the ones based on continuous potentials, especially for low to moderate densities. In contrast to time-stepping methods, simulations based on a discrete potential are *event driven*, namely, the time of the next collision is determined *a priori* and the system is therefore analytically integrated to the time at which the next 'event' occurs, all within a single numerical time step. This distinguished feature permits one to consider systems with larger number of atoms and/or longer simulation time.

In the present work, Event-Driven Molecular Dynamics (EDMD) simulations was carried out for a system of hard spheres. The number of particles was set not less than 4×10^4 and the cross section $x \times y$ was determined so as to match the target density η. Initially, particle spheres are distributed randomly in a computational domain, ensuring that they do not overlap. The initial velocities are sampled from the Maxwell distribution by using the Box-Muller algorithm. The most computationally demanding part of the simulation is to compute the collision times of each pair. The earliest collision is then identified and the simulation jumps to this 'event'. The velocities of all particles are then updated by considering the effect of the external constant force acted upon them during the considered time interval and the post-collisional velocities of the collision pair are computed according to the hard-sphere dynamics. Note that inter-molecular

collisions are not the only form of interaction that particles encounter. It may be possible that the nearest collision of a particle is not with another particle but rather the wall. In the following simulations, walls are considered rough and the Maxwell scattering kernel with perfect accommodation is considered. Just like the Enskog simulations, the EDMD system evolution was followed until a steady state was obtained, by letting the transient behaviour evolve into the time-independent solution. The calculation of the macroscopic quantities commenced after a steady state has been reached through weighted averages of the particles' properties.

D. PHS-MD solver

The pseudo-hard-sphere Molecular Dynamics (PHS-MD) solver is equivalent to the EDMD solver, although it avoids tracking to 'events', it instead tracks using MD's standard Verlet algorithm with a fixed time step. This method is more computationally demanding, but the time step can be chosen to ensure the stability of the model. Furthermore, while our previous two codes were both developed in house, the PHS-MD simulations were performed using the open source Large-scale Atomic/Molecular Massively Parallel (LAMMPS) MD software[53]. The scope of this section is therefore to provide an external, independent means of reproducing our results, although at a higher computational cost.

Similar to EDMD and Enskog simulations, the PHS-MD also uses the same diffusive boundary conditions at the mathematical walls, which is implemented as a new reflective-wall 'fix' in the LAMMPS software. Furthermore, while LAMMPS does not have a hard-sphere interaction potential, we reconcile this by isolating the repulsive part of the (12,6) Lennard Jones (LJ) potential. The standard LJ potential is given by:

$$U_{\mathrm{LJ}}(r) = 4\varepsilon\left[\left(\frac{\sigma}{r}\right)^{12} - \left(\frac{\sigma}{r}\right)^{6}\right], \qquad (7)$$

where r is the separation between two atoms, σ is the length scale parameter (equivalent, approximately, to the diameter of an atom), and ε is the energy well depth of the potential. It is common for LJ potentials to be terminated and shifted at a cut-off distance $r = r_c \sim 3$–$4\ \sigma$ to account for long range interactions.

A well-known application of the LJ potential to hard-sphere interactions was initially suggested by Weeks *et al.*[55], known as the Weeks-Chandler-Andersen potential (WCA), and is given by:

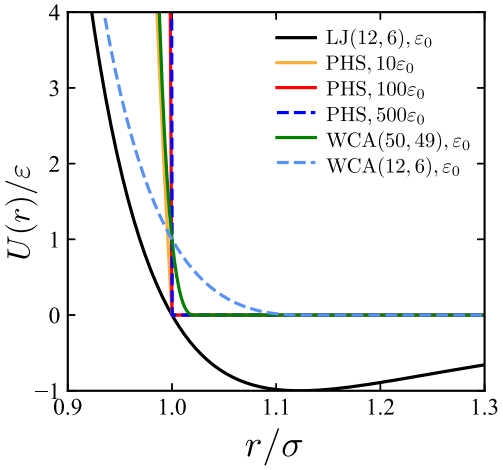

FIG. 2. The pseudo-hard-sphere (PHS) interaction potential as a function of pair-atomic distance r, used in this work. The potential is compared with the standard (12,6) LJ equation with ε_0 and r_c = 2.4 σ; the standard WCA potential, which is a (12,6) LJ potential shifted by ε_0 and cut at $r_c = 2^{1/6}\sigma$; the (50,49) WCA potential used in Ref.[54], with $r_c = (50/49)\sigma$. The PHS is a standard LJ potential with larger ε_0 (as indicated) and cut-off at r_c = σ = 3.4 Å. In this work we use PHS with $100\varepsilon_0$.

$$U_{\mathrm{WCA}}(r) = \begin{cases} U_{\mathrm{LJ}}(r) + \varepsilon_0, & \text{if } r < 2^{1/6}\sigma, \\ 0, & \text{if } r \geq 2^{1/6}\sigma, \end{cases} \qquad (8)$$

which is the LJ potential shifted by the well depth ε_0 and cut off at the minima of the energy well at $r_c = 2^{1/6}\sigma$, as shown in Fig. 2. The properties of a WCA fluid are often used to represent an approximate hard-sphere system due to the steepness of the potential, and no attractive energy. However, this approximation does not always hold, as it will depend in great measure on the kinetic energy of the colliding atoms, or equivalently, on the temperature of the system[54]. In 2012, Jover *et al.*[54] pointed out that the traditional WCA potential does not provide the correct system temperature. They proposed a (50,49) form of the WCA potential, with $r_c = (50/49)\sigma$, containing a small smooth repulsive part which rapidly changes to a very steep energy gradient, as shown in Figure 2, and found some improvement on the hard-sphere dynamics.

Considering that the simulations in the present work are at a relatively high reduced temperature $T^* = k_B T/\varepsilon_0 = 2.47$ in comparison with the results of Jover *et al.*[54], we choose to adopt a pseudo-hard-sphere (PHS) potential. The PHS potential, is also derived

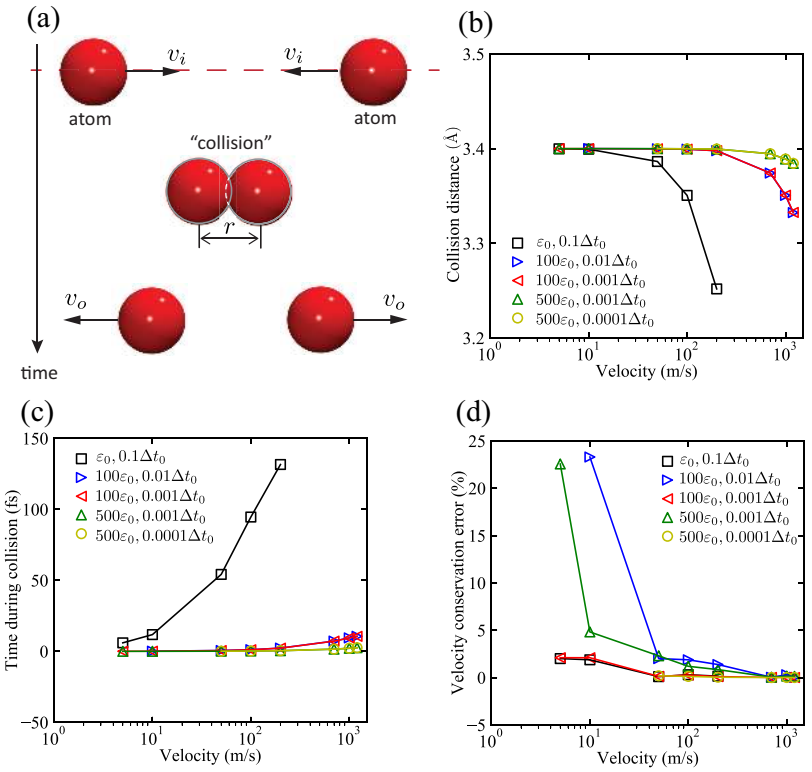

FIG. 3. Two-atom verification tests on PHS parameters ε and Δt. (a) Two atoms are collided at the same initial speed v_i along a central axis. Measurements are taken for: (b) the minimum distance achieved between atoms during collision, (c) the time taken during collision, and (d) the percentage conservation error between initial and post-collision velocities v_i, v_o. Our choice of PHS parameters in this work are $\varepsilon = 100\varepsilon_0$ and $\Delta t = 0.001\Delta t_0$.

from the standard LJ potential, but we further increase the steepness of the energy gradient, by using a very large value of well-depth $\varepsilon = 100\varepsilon_0$, cut the potential at exactly the atom diameter $r_c = \sigma$ to avoid any smoothness in the repulsive part of the potential, and choose a much smaller value of integration time-step $\Delta t = 0.001\Delta t_0$, to maintain numerical stability and avoid fluid heating or simulation 'blow-up'. Here, σ = 3.4 Å, $\varepsilon_0 = 0.239$ Kcal/mol and $\Delta t_0 = 2$ fs are the nominal parameters for a simple fluid such as argon, which we use in this work. The quasi-hard-sphere shape of the PHS potential used in this work is shown in Fig. 2, and indicated by the label 'PHS, 100 ε_0'.

The PHS parameters were chosen using a two-atom collision simulation test, as shown in Fig. 3, and subsequently verified by recovering the thermodynamic properties of hard-sphere systems[44,56,57], as shown in Fig. 4 for pressure vs. density and viscosity vs. density. Fig. 3 shows that for the choice of PHS parameters, the collision diameter is preserved at high speeds and the pre/post collision error in velocity is comparable to standard LJ collisions. However, the overall simulations are much more computationally costly than standard MD due to using a much smaller integration time step. We found that for the few number of atoms employed in this work, these PHS-MD simulations were all practically run on a high-performance computer.

III. RESULTS AND DISCUSSIONS

In order to evaluate the effect of high densities and tight confinements on flow through slit geometries, we measure density, velocity and temperature profiles for all three models and all combinations of simulations for R and η_0. These results will be compared and discussed in this section.

The driving force has been chosen for all cases presented next to ensure that the response to the forcing remains in the linear regime. Linearity no longer holds when the heat caused by viscous dissipation cannot be dissipated through the diffusive boundary conditions. Therefore all profiles presented in this section have been verified to satisfy isothermal conditions. The results for the non-linear regime are presented sepa-

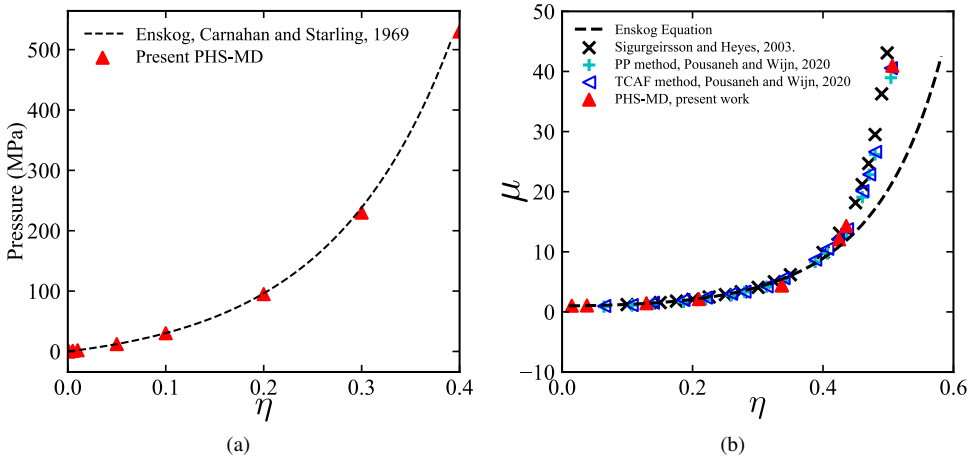

FIG. 4. Verification of (a) pressure and (b) dimensionless viscosity μ as a function of reduced density η for our PHS-MD simulations with literature. Viscosity measurements in (b) were obtained using a simple Couette flow simulation, which involves setting the velocities of bottom and upper walls, separated by a distance of 200 nm, at -50 m/s and +50 m/s, respectively. Both walls are modelled using the diffuse wall boundary condition. The viscosity is then calculated using Newton's law of viscosity, with shear stress and velocity gradient measured from the channel.

rately in Appendix A as a further verification of agreement between the three numerical methods employed.

A. Density and velocity profiles

Macroscopic quantities across the channel are shown for a representative set of confinement ratio and reference reduced densities, i.e. $R = [10, 5, 2]$ and $\eta_0 = [0.01, 0.1, 0.3]$. These cases are selected to cover a significant range of Knudsen numbers (i.e. from slip to early transition regime) and specifically highlight the peculiar features of fluids when dense effects and confinement come into play.

For a relatively loose confinement, $R = 10$, when the reference reduced density is small, $\eta_0 = 0.01$ (Fig. 5(a)), we can see all the three methods predict a fluid ordering near the surface at z/σ = 4.5, with a peak of about 1.15, while the predominant fluid being bulk. When the reference reduced density is increased to 0.1 and 0.3, as shown in Figs. 5(b),(c), we can see more fluid ordering starting to penetrate into the bulk fluid with two and three layers observed in the density profiles, respectively, with the largest peak closer to the surface. In all three models, there is very good agreement at the lower reference reduced densities, while the Enskog starts to show initial signs of small deviations from EDMD and PHS-MD at the largest reference reduced density considered ($\eta_0 = 0.3$), in the magnitude and location of the peaks of the layers. This is not unexpected, as the Enskog solution is known to provide accurate predictions of hard-sphere systems only up to moderate values of reduced density[57], as seen in Fig. 4(b). For the velocity profiles (see Figs. 5(d)–(f)), the agreement between the three models is also very good, with noticeable slippage at the walls, and indications of non-parabolic behaviour.

Figures 6(a)–(f) shows the density and velocity profiles for the higher confined case of $R = 5$. We can make a similar comparison. Fluid ordering in the density profiles are similar to $R = 10$ with the values of the peak for the first layer being similar, but the density layering occupying more of the fluid bulk. Velocity profiles exhibit more pronounced non-continuum behaviour, as observed from the inflection points and plug-like profiles.

When the channel height is reduced to $R = 2$, a distinct heterogeneous distribution of density is observed, as shown in Figs. 7 (a)–(c). It is clear that the ordering now occurs throughout the channel, distinct of two layer ordering in the highest reference reduced density, $\eta_0 = 0.3$, while velocity profiles are indicative of quasi plug flow.

In summary, the Enskog equation is found to be able to capture the density and velocity profiles quite well when compared with the molecular dynamics simulations, although slight discrepancies are observed at the highest densities, in particular with errors in capturing the ordering at the midpoint of the channel in the high confined cases.

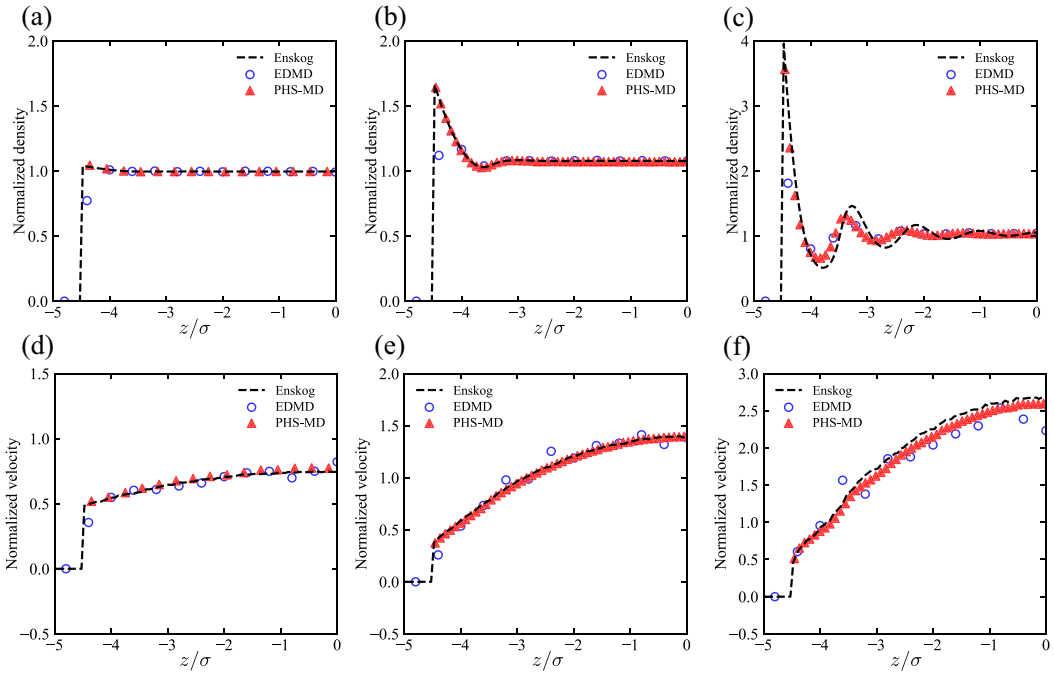

FIG. 5. Profiles of (a), (b), (c) normalized reduced density (top) and (d), (e), (f) normalised velocity (bottom) for gas flow with η_0=0.01, 0.1, 0.3 (columns: left to right) in the channel of R=10.

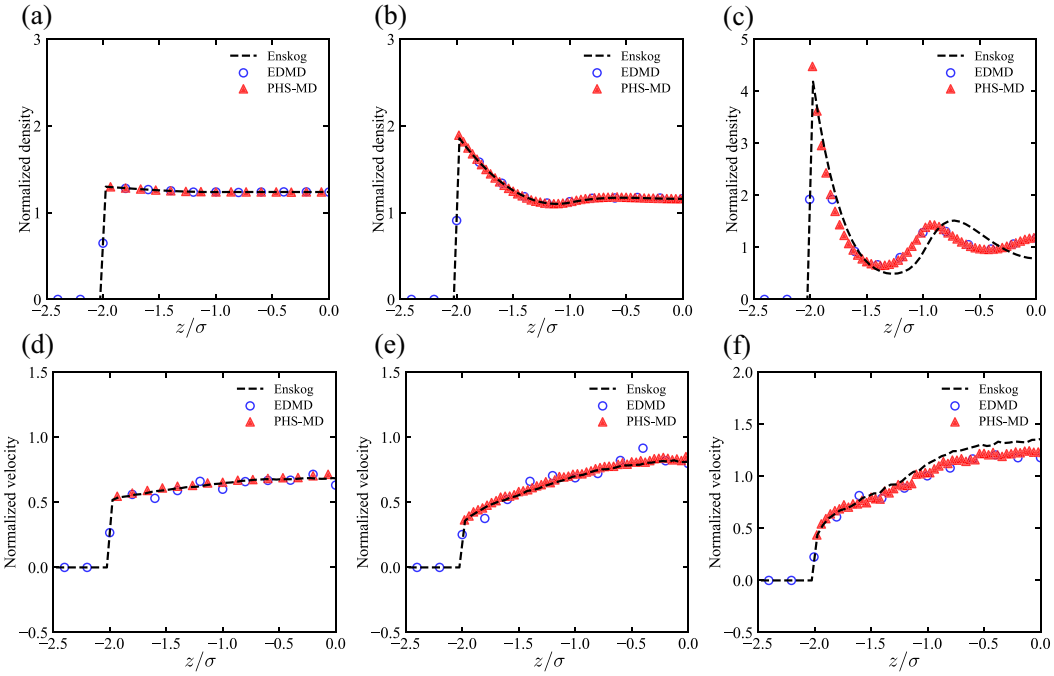

FIG. 6. Profiles of (a), (b), (c) normalized reduced density (top) and (d), (e), (f) normalised velocity (bottom) for gas flow with η_0=0.01, 0.1, 0.3 (columns: left to right) in the channel of R=5.

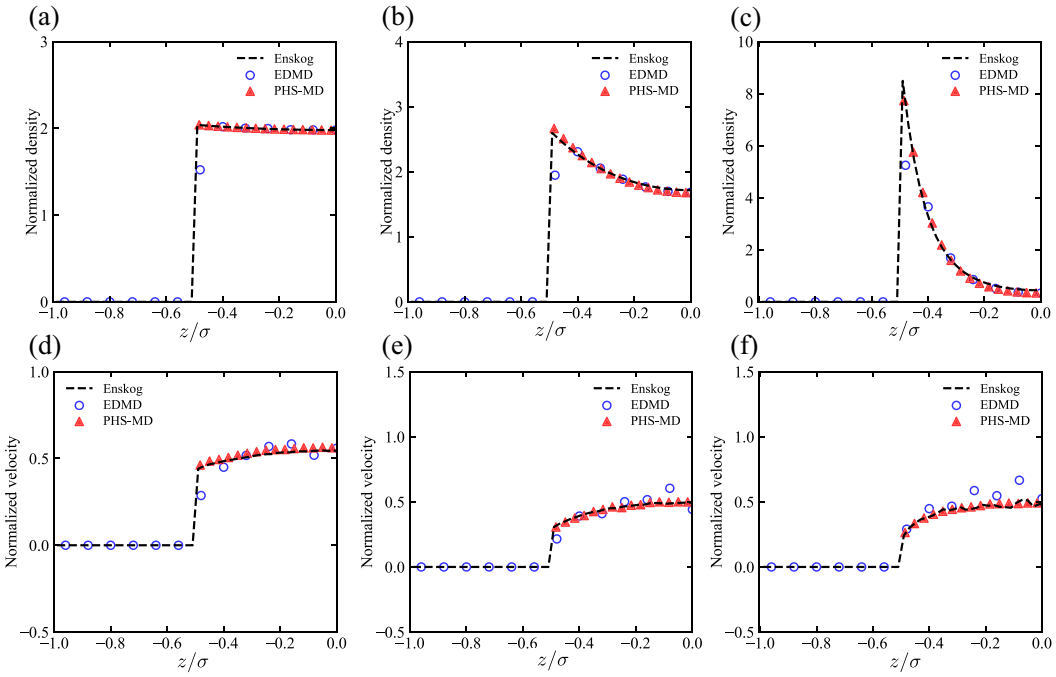

FIG. 7. Profiles of (a), (b), (c) normalized reduced density (top) and (d), (e), (f) normalised velocity (bottom) for gas flow with η_0=0.01, 0.1, 0.3 (columns: left to right) in the channel of R=2.

B. Flow response with confinement

The normalized mass flow rates for a dense gas in ultra-tight confinement and in the linear flow response regime are shown in Fig. 8. The mass flow rate was measured as a spatial integration of local density, area and velocity, using discretised bins along the z direction. The normalization for mass flow rate is described in more detail in Appendix B. To illustrate the influence of confinement and density, we compare our results with the linearized Boltzmann solution by Ohwada *et al.*[58], which is only applicable to $R \to \infty$, and the slip Poiseuille mass flow rate prediction, which represents the limit of $Kn \to 0$. Other methods are shown to predict the full extent of this Kn range, such as the efficient DSBGK method[9] .

Of all results in our parametric study, the results for the lowest confinement R = 20 captures the best approximation to the standard Knudsen minimum curve of Ohwada *et al.*[58], especially when Kn is large (i.e. within the transition and free molecular flow regimes). When $Kn > 0.1$ the normalized mass flow rate is less than the Knudsen minimum curve by about 5%, which should be attributed to the slight confinement that exists. However, when $Kn < 0.1$, there is a noticeable reduction in mass flow rate compared with the original non-confined Knudsen minimum curve. Overlapping results were obtained for a few data points with larger

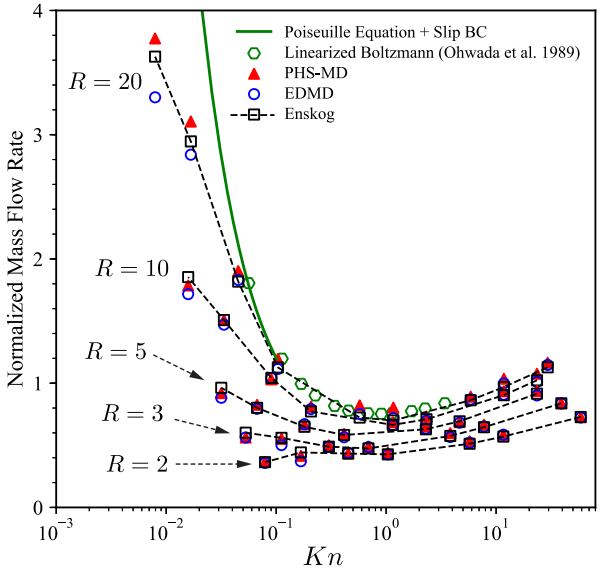

FIG. 8. Dependance of normalized mass flow rate on gas rarefaction Kn and confinement R.

$R \sim 100$.

When the channels are reduced from R = 20, 10, 5, 3 to 2, a flattening of the minimum curve (or a disappearance of the Knudsen minimum, as indicated in Ref.[43]) and a shift in the curves downwards at larger

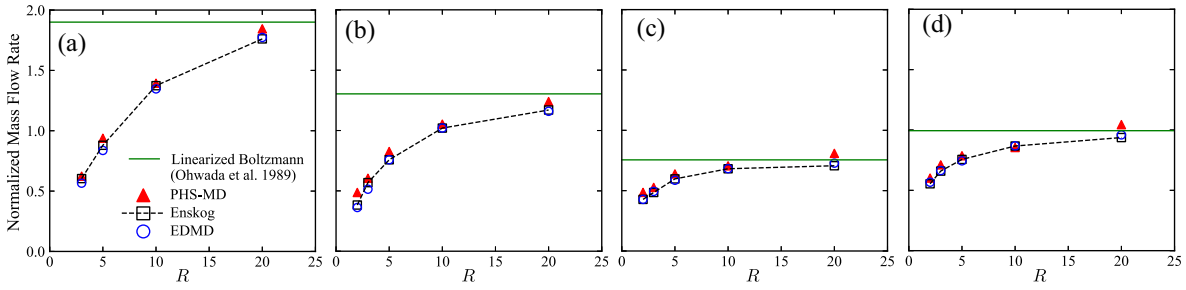

FIG. 9. Dependance of normalized mass flow rate on confinement R for Knudsen numbers (a) $Kn = 0.05$, (b) $Kn = 0.1$, (c) $Kn = 1$ and (d) $Kn = 10$.

Kn are also observed with the proposed normalisation, which is not unexpected. While visual comparison seems to indicate different trends between our results and those of Wu *et al.*[43], this is only due to the different normalisation schemes adopted across these two studies; we confirm that the dimensional values for flow rate per unit width are the same for all R and Kn considered in[43]. The normalisation for $R = H/\sigma$ in this work is taken to be the actual wall-to-wall channel height (as is illustrated in the set-up of Fig. 1), while in Wu *et al.*[43], the height is taken from the midpoint of those atoms upon collision with the walls (i.e. $R = (H-\sigma)/\sigma$). The reason this is important is that in the dilute-gas Boltzmann limit, molecules are treated as point-like masses, and as such, they can fill the whole channel. By contrast, the space available to molecules in a confined channel is $H-\sigma$ if their finite size is accounted for. As the confinement ratio reduces, this mismatch between nominal and effective channel widths becomes more and more important, as we demonstrate in Fig. 8, and eventually, it leads to a mass flow rate which is smaller than the one predicted based on the Boltzmann equation. This explains why there should be downward shifts in the Knudsen minimum curve as $R \to 2$.

Deviations from the Knudsen minimum curve are seen more clearly in Figure 9, with the larger deviations occurring in the dense gas region (low Kn), that cannot be fully explained by just changes in our normalisation for R. Note also that, to some extent, the effect of the increasing viscosity at small Kn is already taken into account by including the pressure in the normalisation factor of the mass flow rate. Even reverting to the normalisation of Wu *et al.*[43], reveal these large deviations for $Kn \to 0$ remain.

In the original explanation of the Knudsen minimum, there is a trade-off between two competing mechanisms: viscous dissipation at $Kn \to 0$ and Knudsen diffusion when $Kn \to \infty$[16,17]. Our simulation results suggest that the molecular ordering of dense gases under tight confinement now play an added role, such that there is a larger non-continuum viscous dissipation in the limit of $Kn \to 0$, which leads to a drop in the overall flow response (i.e. a higher flow resistivity). As the confinement increases, the width of the bulk region reduces and eventually disappears. Accordingly, the viscosity of the fluid is expected to be different from the nominal one [19–22]. It is possible that this and other effects (e.g. surface and Knudsen diffusion) could be playing a role. The interplay between these effects are at this stage unclear, and require a deeper fundamental study in this area.

IV. CONCLUSIONS

The main scope of this paper has been to verify the phenomena of the Knudsen minimum disappearance observed in a recent publication based on the Enskog equation[43]. A validation study was necessary to clarify whether or not that conclusion depended on the approximations behind the kinetic theory treatment of the hard-sphere collision dynamics. We studied the force-driven Poiseuille flow by using three very different approaches: the Enskog equation, solved by using a stochastic Monte Carlo scheme, Event-Driven Molecular Dynamics (EDMD), and pseudo-hard-sphere Molecular Dynamics (PHS-MD). The PHS-MD simulations were carried out by using the popular LAMMPS software for external reproducibility of our simulation results. Density, velocity, and overall flow rate showed agreement between EDMD, PHS-MD and the Enskog solutions. Furthermore deviations and flattening of the mass flow rate versus Knudsen curves were verified with increases in density and in tight confinement of the gas. At very high reference reduced densities, corresponding to $\eta_0 \sim 0.3$, we found that the Enskog equation begins to deviate from the MD-based solutions, indicating possible breakdown, although these deviations remain small. In porous media applications, such as in shale gas, the practical reduced density limit oc-

curring in these reservoir conditions is $\bar{\eta} < 0.2$, arising from pressures less than 100 MPa. In addition, we find that in terms of computational cost, the Enskog solver outperforms the MD solvers by 3 orders of magnitude for the EDMD and 4 orders of magnitude for the PHS-MD. This paper therefore raises the applicability and profile of the Enskog equation to deal with these porous media problems. Further studies are required to investigate the underpinning causes of this anomalous flow response behaviour, as well as systematically investigate the effects of long range interactions, realistic potentials, and realistic surfaces with chemical specificity, that replace the basic hard-sphere collisions and diffusive walls considered in this work. The Enskog equation can also be developed for 3D geometries, and modified to handle complex multiphase flows in porous media, such as in the Enskog-Vlasov formalism[29–31,59].

ACKNOWLEDGEMENTS

The authors would like to dedicate this article to Jason Reese, our mentor, colleague, and friend, who passed away in March 2019.

This work is financially supported by King Fahd University of Petroleum and Minerals (KFUPM), Saudi Arabia. Our MD simulations were performed on ARCHER, the UK's national supercomputer. The authors thank Dr Peng Wang (HUST) and Dr Lei Wu (SUSTech) for useful discussions.

A: Results for gas flows in non-linear regime

In Figure 10 and 11 we show a small sample of simulations results. More specifically, a comparison is shown between Enskog, EDMD and PHS-MD, for R = 4 and 10, respectively. The scope is to demonstrate the good agreement that still exists across the methods in the non-linear flow response regime, i.e. when the forcing is too high for heat to be dissipated; this is evident by the normalized temperature profile being larger than one.

B: Reference quantities

In the present work, the number density is made dimensionless by using a reference number density, n_0, and the velocity by using the reference flow speed, V_0, assumed to be proportional to the mean molecular velocity:

$$V_0 = \frac{n_0 F_0 H}{p_0}\left(\frac{2k_B T_0}{m}\right)^{1/2}, \tag{B1}$$

where k_B is the Boltzmann constant, m the molecular mass, F_0 is the constant force applied on each atom to simulate the Poiseuille flow, H the channel height, and p_0 is the reference pressure, related to reference density and temperature through the Carnahan and Starling equation of state:

$$\frac{p_0}{n_0 k_B T_0} = \frac{1+\eta_0+\eta_0^2-\eta_0^3}{(1-\eta_0)^3}, \qquad \eta_0 = \frac{\pi\sigma^3 n_0}{6}. \tag{B2}$$

Note that the pressure is included in Eq. (B1) to account for the fluid compressibility. This choice permits one to rule out the effects of the different fluid bulk properties at high densities.

Likewise, the reference mass flow rate per unit of time is defined as follows:

$$Q_0 = \rho_0 V_0 H D, \tag{B3}$$

where D is the depth of the channel and $\rho_0 = m n_0$. By substituting Eq. (B1) into Eq. (B3), the reference mass flow rate per unit of time reads:

$$Q_0 = \frac{\rho_0 n_0 F_0 H^2 D}{p_0}\left(\frac{2k_B T_0}{m}\right)^{1/2}. \tag{B4}$$

The reference state is taken to be the argon gas at T_0=298 K, i.e. $m = 6.63\times10^{-23}$ g, $\sigma = 3.4\times10^{-10}$ m.

DATA AVAILABILITY

The data that support the findings of this study are openly available at http://doi.org/[doi] *(DOI to be included at proofs stage).*

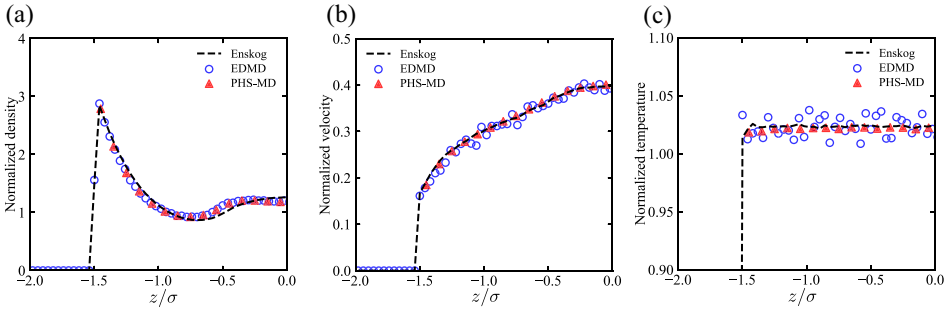

FIG. 10. Profiles of (a) normalized reduced densities, (b) normalised velocity and (c) normalised temperature for gas flow with $\eta_0 = 0.2$ in R=4; $\tilde{F} = 0.2$.

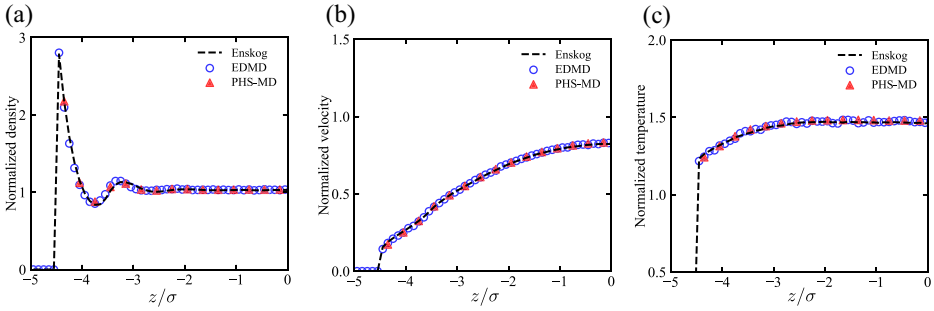

FIG. 11. Profiles of (a) normalized reduced densities, (b) normalised velocity and (c) normalised temperature for gas flow with $\eta_0 = 0.2$ in R=10; $\tilde{F} = 0.2$.

REFERENCES

[1] J. K. Holt, H. G. Park, Y. Wang, M. Stadermann, A. B. Artyukhin, C. P. Grigoropoulos, A. Noy, and O. Bakajin, "Fast mass transport through sub-2-nanometer carbon nanotubes," Science (USA) **312**, 1034–1037 (2006).

[2] Y. Gensterblum, A. Ghanizadeh, R. J. Cuss, A. Amann-Hildenbrand, B. M. Krooss, C. R. Clarkson, J. F. Harrington, and M. D. Zoback, "Gas transport and storage capacity in shale gas reservoirs – a review. part a: Transport processes," Journal of Unconventional Oil and Gas Resources **12**, 87 – 122 (2015).

[3] G. M. Kremer, *An introduction to the Boltzmann equation and transport processes in gases* (Springer Science & Business Media, 2010).

[4] W.-M. Zhang, G. Meng, and X. Wei, "A review on slip models for gas microflows," Microfluidics and Nanofluidics **13**, 845–882 (2012).

[5] L. Zhang, S. Baochao, Z. Yulong, and G. Zhaoli, "Review of micro seepage mechanisms in shale gas reservoirs," International Journal of Heat and Mass Transfer **139**, 144–179 (2019).

[6] H. Struchtrup, "Macroscopic transport equations for rarefied gas flows," in *Macroscopic Transport Equations for Rarefied Gas Flows* (Springer, 2005) pp. 145–160.

[7] M. Torrilhon, "Modeling nonequilibrium gas flow based on moment equations," Annual Review of Fluid Mechanics **48**, 429–458 (2016).

[8] G. A. Bird, *Molecular Gas Dynamics and the Direct Simulation of Gas Flows* (Clarendon Press: Oxford, 1994).

[9] J. Li, *Multiscale and Multiphysics Flow Simulations of Using the Boltzmann Equation* (Springer, 2020).

[10] J. Li, "Efficient prediction of gas permeability by hybrid DSBGK-LBM simulations," Fuel **250**, 154–159 (2019).

[11] R. S. Myong, A. Karchani, and O. Ejtehadi, "A review and perspective on a convergence analysis of the direct simulation monte carlo and solution verification," Physics of Fluids **31**, 066101 (2019).

[12] M. H. Ahmadian, E. Roohi, A. Teymourtash, and S. Stefanov, "A dusty gas model-direct simulation monte carlo algorithm to simulate flow in micro-porous media," Physics of Fluids **31**, 062007 (2019).

[13] G. Dimarco and L. Pareschi, "Numerical methods for kinetic equations," Acta Numerica **23**, 369–520 (2014).

[14] G. P. Ghiroldi and L. Gibelli, "A direct method for the Boltzmann equation based on a pseudo-spectral velocity space discretization," Journal of Computational Physics **258**, 568–584 (2014).

[15] C. Cercignani and A. Daneri, "Flow of a rarefied gas between two parallel plates," Journal of Applied Physics **34**, 3509–3513 (1963).

[16] W. Pollard and R. D. Present, "On gaseous self-diffusion in long capillary tubes," Physical Review **73**, 762 (1948).

[17] G. Tatsios, S. K. Stefanov, and D. Valougeorgis, "Predicting the knudsen paradox in long capillaries by decomposing the flow into ballistic and collision parts," Physical Review E **91**, 061001 (2015).

[18] S. A. Somers and H. T. Davis, "Microscopic dynamics of fluids confined between smooth and atomically structured solid surfaces," Journal of Chemical Physics **96**, 5389–5407 (1992).

[19] K. P. K. Travis, B. D. B. Todd, and D. D. J. Evans, "Departure from Navier-Stokes hydrodynamics in confined liquids," Physical Review E **55**, 4288–4295 (1997).

[20]B. D. Todd and D. J. Evans, "Temperature profile for Poiseuille flow," Physical Review E **55**, 2800–2807 (1997).
[21]K. P. Travis, B. D. Todd, and D. J. Evans, "Poiseuille flow of molecular fluids," Physica A: Statistical and Theoretical Physics **240**, 315 – 327 (1997).
[22]K. P. Travis and K. E. Gubbins, "Poiseuille flow of Lennard-Jones fluids in narrow slit pores," Journal of Chemical Physics **112**, 1984–1994 (2000).
[23]H. W. Kim, H. W. Yoon, S.-M. Yoon, B. M. Yoo, B. K. Ahn, Y. H. Cho, H. J. Shin, H. Yang, U. Paik, S. Kwon, J.-Y. Choi, and H. B. Park, "Selective gas transport through few-layered graphene and graphene oxide membranes," Science **342**, 91–95 (2013).
[24]L. Zhang, B. Zhao, C. Jiang, J. Yang, and G. Zheng, "Preparation and transport performances of high-density, aligned carbon nanotube membranes," Nanoscale Research Letters **10**, 970 (2015).
[25]J. H. Ferziger, H. G. Kaper, and H. G. Kaper, *Mathematical theory of transport processes in gases* (North-Holland, 1972).
[26]H. Ted Davis, "Kinetic theory of flow in strongly inhomogeneous fluids," Chemical Engineering Communications **58**, 413–430 (1987).
[27]X.-D. Din and E. E. Michaelides, "Kinetic theory and molecular dynamics simulations of microscopic flows," Physics of Fluids **9**, 3915–3925 (1997).
[28]S. V. Nedea, A. J. Frijns, A. A. van Steenhoven, A. Jansen, A. J. Markvoort, and P. A. Hilbers, "Density distribution for a dense hard-sphere gas in micro/nano-channels: Analytical and simulation results," Journal of Computational Physics **219**, 532–552 (2006).
[29]A. Frezzotti, L. Gibelli, and S. Lorenzani, "Mean field kinetic theory description of evaporation of a fluid into vacuum," Physics of Fluids **17**, 12102 (2005).
[30]A. Frezzotti, L. Gibelli, D. Lockerby, and J. Sprittles, "Mean-field kinetic theory approach to evaporation of a binary liquid into vacuum," Physical Review Fluids **3**, 054001 (2018).
[31]A. Frezzotti, P. Barbante, and L. Gibelli, "Direct simulation monte carlo applications to liquid-vapor flows," Physics of Fluids **31**, 062103 (2019).
[32]P. Barbante, A. Frezzotti, and L. Gibelli, "A kinetic theory description of liquid menisci at the microscale," Kinetic & Related Models **8**, 235 (2015).
[33]A. Rahman, "Correlations in the motion of atoms in liquid argon," Physical Review **136**, A405 (1964).
[34]L. Verlet, "Computer "Experiments" on Classical Fluids. I. Thermodynamical Properties of Lennard-Jones Molecules," Physical Review **159**, 98 (1967).
[35]B. J. Alder and T. E. Wainwright, "Studies in molecular dynamics. i. general method," The Journal of Chemical Physics **31**, 459–466 (1959).
[36]J. R. Henderson and F. van Swol, "On the interface between a fluid and a planar wall," Molecular Physics **51**, 991–1010 (1984).
[37]A. Frezzotti, "Monte Carlo simulation of the heat flow in a dense hard sphere gas," European Journal of Mechanics-B/Fluids **18**, 103 – 119 (1999).
[38]J. Mittal, J. R. Errington, and T. M. Truskett, "Thermodynamics predicts how confinement modifies the dynamics of the equilibrium hard-sphere fluid," Physical Review Letters **96**, 177804 (2006).
[39]G. Goel, W. P. Krekelberg, J. R. Errington, and T. M. Truskett, "Tuning density profiles and mobility of inhomogeneous fluids," Physical Review Letters **100**, 106001 (2008).
[40]M. Barisik and A. Beskok, "Scale effects in gas nano flows," Physics of Fluids **26**, 052003 (2014).
[41]S. Mandal and T. Franosch, "Diverging time scale in the dimensional crossover for liquids in strong confinement," Physical Review Letters **118**, 065901 (2017).
[42]K. Ghosh and C. V. Krishnamurthy, "Structural behavior of supercritical fluids under confinement," Physical Review E **97**, 012131 (2018).
[43]L. Wu, H. Liu, J. M. Reese, and Y. Zhang, "Non-equilibrium dynamics of dense gas under tight confinement," Journal of Fluid Mechanics **794**, 252–266 (2016).
[44]N. F. Carnahan and K. E. Starling, "Equation of state for nonattracting rigid spheres," Journal of Chemical Physics **51**, 635–636 (1969).
[45]H. v. Beijeren and M. H. Ernst, "The modified Enskog equation," Physica **68**, 437–456 (1973).
[46]J. Fischer and M. Methfessel, "Born-Green-Yvon approach to the local densities of a fluid at interfaces," Physical Review A **22**, 2836 (1980).
[47]A. Frezzotti, "A particle scheme for the numerical solution of the Enskog equation," Physics of Fluids **9**, 1329–1335 (1997).
[48]M. P. Allen, D. Frenkel, and J. Talbot, "Molecular dynamics simulation using hard particles," Computer Physics Reports **9**, 301–353 (1989).
[49]A. Donev, "Asynchronous event-driven particle algorithms," Simulation **85**, 229–242 (2009).
[50]M. N. Bannerman, R. Sargant, and L. Lue, "Dynamo: a free $\mathcal{O}$(N) general event-driven molecular dynamics simulator," Journal of Computational Chemistry **32**, 3329–3338 (2011).
[51]G. A. Chapela, L. Scriven, and H. Davis, "Molecular dynamics for discontinuous potential. IV. Lennard-Jonesium," The Journal of Chemical Physics **91**, 4307–4313 (1989).
[52]J. R. Elliott Jr, "Optimized step potential models for n-alkanes and benzene," Fluid Phase Equilibria **194**, 161–168 (2002).
[53]S. Plimpton, "Fast parallel algorithms for short-range molecular dynamics," Journal of Computational Physics **117**, 1–19 (1995).
[54]J. Jover, A. J. Haslam, A. Galindo, G. Jackson, and E. A. Müller, "Pseudo hard-sphere potential for use in continuous molecular-dynamics simulation of spherical and chain molecules," The Journal of Chemical Physics **137**, 144505 (2012).
[55]J. D. Weeks, D. Chandler, and H. C. Andersen, "Role of repulsive forces in determining the equilibrium structure of simple liquids," The Journal of Chemical Physics **54**, 5237–5247 (1971).
[56]F. Pousaneh and A. S. de Wijn, "Shear viscosity of pseudo hard-spheres," Molecular Physics **118**, 1622050 (2020).
[57]H. Sigurgeirsson and D. M. Heyes, "Transport coefficients of hard sphere fluids," Molecular Physics **101**, 469–482 (2003).
[58]T. Ohwada, Y. Sone, and K. Aoki, "Numerical analysis of the poiseuille and thermal transpiration flows between two parallel plates on the basis of the boltzmann equation for hard-sphere molecules," Physics of Fluids A: Fluid Dynamics **1**, 2042–2049 (1989).
[59]M. Sadr and M. H. Gorji, "A continuous stochastic model for non-equilibrium dense gases," Physics of Fluids **29**, 122007 (2017).